IEEE Photonics Journal
An IEEE Photonics Society Publication

Open Access

Ultrahigh *Q* Polymer Microring Resonators for Biosensing Applications

Volume 11, Number 2, April 2019

Xin Tu
Sung-Liang Chen
Chaolong Song
Tianye Huang
L. Jay Guo

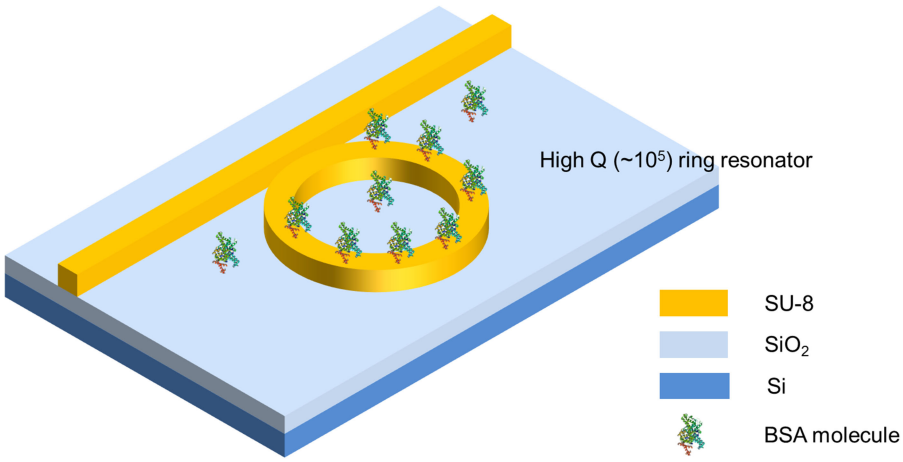

DOI: 10.1109/JPHOT.2019.2899666
1943-0655 © 2019 IEEE

Ultrahigh *Q* Polymer Microring Resonators for Biosensing Applications

Xin Tu,[1] **Sung-Liang Chen**,[2] **Chaolong Song**,[1] **Tianye Huang**,[1] **and L. Jay Guo**[3]

[1]School of Mechanical Engineering and Electronic Information, China University of Geosciences, Wuhan 430074, China
[2]University of Michigan–Shanghai Jiao Tong University Joint Institute, Shanghai Jiao Tong University, Shanghai 200240, China
[3]Department of Electrical Engineering and Computer Science, University of Michigan, Ann Arbor, Michigan 48109, USA

DOI:10.1109/JPHOT.2019.2899666

Manuscript received December 14, 2018; revised February 7, 2019; accepted February 12, 2019. Date of publication February 15, 2019; date of current version March 5, 2019. This work was supported by Wuhan Municipal Science and Technology Bureau under Grant 2018010401011297. Corresponding authors: Tianye Huang and L. Jay Guo (e-mail: tianye_huang@163.com; guo@umich.edu).

Abstract: The capability of an ultrahigh *Q* polymer microring resonator as a biosensing system is systematically investigated. By optimizing the device design and fabrication process, the device operates in the slightly under-coupled regime with a record intrinsic *Q* factor of 8.0×10^5, which offers a high sensitivity and low detection limit. In surface mass detection, a surface mass density of 12.7 pg/mm^2 of bovine serum albumin is detected due to the physical adsorption. The noise-equivalent detection limit is approximately 5.3 pg/mm^2 in a wavelength-shift scheme and 55.9 fg/mm^2 in an intensity-variation scheme. These results show that the best sensing performance with the on-chip polymer ring resonator system is achieved.

Index Terms: Biosensor, ring resonator.

1. Introduction

Optical micro-resonators are extensively investigated as a promising label-free biosensing tool for applications in medical diagnosis, environmental monitoring and homeland security [1], [2]. In these micro-resonators, the evanescent fields of the resonant light are utilized to probe the surface mass loading or the refractive index (RI) change caused by the presence of analytes in the surrounding medium. Up to now, sensing performances of the micro-resonators including optical microdisks [3], [4] and microrings [5]–[7], stand-alone microspheres [8] and microtoroids [9], silica micro-capillaries [10] and Fabry-Perot microcavities [11], photonic crystals [12] and grating microcavities [13] have been studied. Among these micro-resonators, whispering gallery mode (WGM)-based resonators as biosensors [14] have drawn a lot of attentions because their higher *Q* factors can offer lower detection limit. In particular, silica microtoroid resonators have *Q* factors of $>10^8$ was claimed to be able to respond to single molecules [9].

On the other hand, on-chip planar integratable microring resonators are good candidates for biosensing systems due to their capability of large-scale integration and mass fabrication [15]. Various materials such as glass [5], titanium dioxide [16], silicon-on-insulator [4], [6], silicon oxynitride

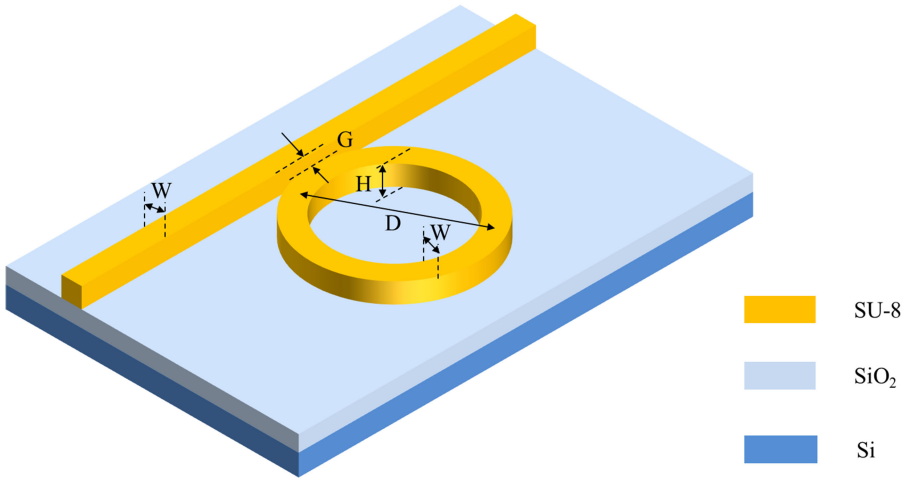

Fig. 1. Schematic of a microring coupled with a bus waveguide.

[17] and polymers (e.g., polystyrene, polymethylmethacrylate, polycarbonate, ZPU13-430, Ormocore and SU-8, etc.) [18]–[26] were employed to fabricate microring resonators. Because of the cheap material and simple fabrication process, polymer biosensors are ideal for disposable uses, which is beneficial to biomedical applications. Moreover, a variety of polymers can be synthesized to render specific properties, including low optical loss, special surface functionalities and biocompatibility. The lower optical loss, i.e., higher *Q*-factor, should be primary focus in order to achieve a lower detection limit. Recently all-polymer microring resonators made of UV-curable Norland optical adhesives, with a measured *Q*-factor of $\sim 5.8 \times 10^4$, were fabricated by cost-effective roll-to-roll nanoimprint lithography (NIL), enabling relatively low bisosensing detection limit [27].

In this paper, we study the high-*Q* SU-8 microring resonators fabricated by NIL for biosensing applications. SU-8 polymer has been widely studied in the field of photonics and microfluidics because of its excellent optical and mechanical properties, high resistance to corrosion and high thermal stability. It has a unique functionality that its high degree of cross-linking can produce the sidewall with straight profiles and high aspect ratios. By UV imprinting the device with a transparent polymer mold which was duplicated from a smooth-sidewall silicon master mold, a record-high intrinsic *Q* factor of $\sim 8.0 \times 10^5$ is achieved. This value is one order of magnitude higher than the highest *Q* factor of polymer microring resonators by UV-NIL technique so far. The use of polymer molds avoided the deterioration of the master during the directly imprint process, and the lower baking temperature was helpful to avoid wafer bending in a large-area NIL process. The device is used for surface mass detection of bovine serum albumin (BSA) molecules of 12.7 pg/mm^2 due to the physical adsorption. The noise-equivalent detection limit (NEDL) is approximately 5.3 pg/mm^2 in a wavelength-shift scheme and 55.9 fg/mm^2 in an intensity-variation scheme. The results show that the ultrahigh-*Q* polymer microring resonators are advantageous for a highly-sensitive biosensing platform.

2. Device Design, Fabrication and Characterization

2.1 Device Design

In order to lower the detection limit, there are several considerations in the design of a microring resonator: high sensitivity, narrow linewidth of the resonance spectrum (i.e., high-*Q* factor), and high signal-to-noise contrast ratios [28]. Fig. 1 shows the schematic of a microring coupled with a bus waveguide. First, the cross section of the waveguide is designed as follows. High sensitivity requires strong interaction between the evanescent wave and the analytes near the waveguide surface,

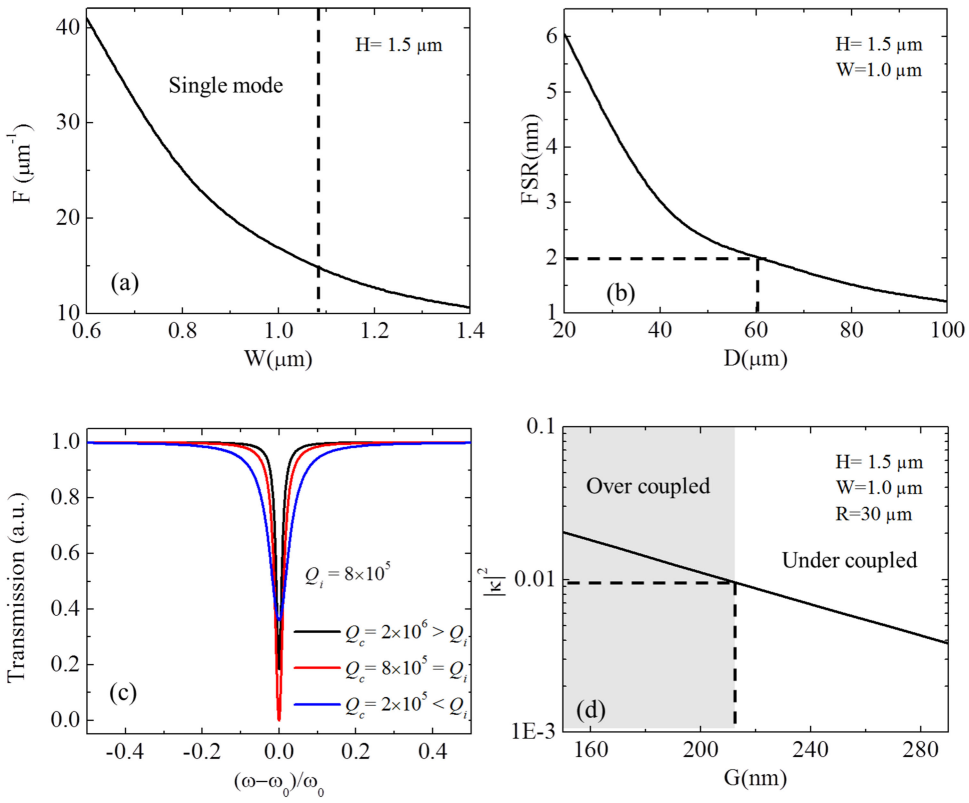

Fig. 2. Illustration of the dependence of the metrics on the structure parameters. (a) The surface sensitivity factor F as a function of the waveguide width W. (b) FSR as a function of diameter D for a 1.5 μm $\times$ 1.0 μm waveguide. (c) The dependence of the transmission spectra on coupling *Q* factors Q_c. (d) The coupling efficiency as a function of gap size G for R = 30 μm, W = 1.0 μm and H = 1.5 μm.

which prefers a smaller waveguide's cross section. However, more evanescent fields outside the smaller cross section of the waveguide result in a higher optical energy loss and thus a lower-*Q* factor. In this regard, the cross section of the waveguide should be optimized by considering the trade-off between the interaction (of the evanescent wave and the analytes) and the *Q* factor. The single-mode propagation is another requirement when designing the waveguide's cross section. It ensures the simple spectrum without unwanted high-order low-*Q* resonance, which facilitates the determination of a resonance shift. Fig. 2(a) presents the surface sensitivity factor F as a function of the waveguide width W. The surface sensitivity factor F is defined as the ratio of the integral of optical intensity over the total surface of the microring to that over the whole space, which is proportional to the surface sensitivity. For a given film thickness H = 1.0 μm, the cross section of the waveguide is designed to be 1.5 μm $\times$ 1.0 μm (height H $\times$ width W) for low loss, high sensitivity and single-mode propagation at 780 nm.

Second, the diameter of the microring is determined as follows. It should be large enough to decrease the bending loss. On the other hand, the larger the diameter of the microring, the narrower the free spectrum range (FSR), which limits the maximum resonance shift that can be recognized and thus the detection range. Typically, for biosensing applications, the diameter of the polymer microring resonator should be smaller than tens of microns to enable the sufficiently wide FSR. Fig. 2(b) presents the FSR as a function of diameter D for a 1.5 μm(H) $\times$ 1.0 μm(W) waveguide. To achieve a FSR of $\sim$2 nm, the diameter of the microring is set to be 60 μm.

Third, the gap size between the microring resonator and the bus waveguide is considered as follows. The signal-to-noise contrast ratio is determined by the contrast between the ON and OFF transmission (ON: off resonance; OFF: at resonance), which is in part affected by the gap size

(i.e., coupling strength). Note that the gap size also affects the overall Q factor through the coupling loss, and thus, it is important to optimize the gap size for high contrast ratio and high Q. The transmission function of a singly coupled microring resonator can be expressed by the following equation according to the coupled mode theory [29]:

$$T = \frac{4\left(\frac{\omega-\omega_0}{\omega_0}\right)^2 + \left(\frac{1}{Q_c} - \frac{1}{Q_i}\right)^2}{4\left(\frac{\omega-\omega_0}{\omega_0}\right)^2 + \left(\frac{1}{Q_c} + \frac{1}{Q_i}\right)^2} \tag{1}$$

where ω is the frequency of the input light, ω_0 is the resonant frequency of the optical mode in the microring resonator, Q_i is the intrinsic Q factor of an isolated microring, and Q_c is the waveguide-to-microring coupling Q factor. Fig. 2(c) shows the Lorentz-shaped transmission curves when $Q_c > Q_i$ (i.e., under coupled), $Q_c = Q_i$ (i.e., critically coupled), and $Q_c < Q_i$ (i.e., over coupled) for the case $Q_i = 8 \times 10^5$. The microring resonator in slightly under-coupled or critically-coupled regimes provides both the high contrast ratio and high Q considering the same Q_i factors. Since Q factor is inversely proportional to the waveguide-to-microring coupling efficiency, the Q factor of $\sim 10^5$ indicates a coupling efficiency of $\sim$0.01 [29]. Fig. 2(d) shows the coupling efficiency $|\kappa|^2$ as a function of gap size G for R = 30 μm, W = 1.0 μm and H = 1.5 μm. Therefore, according to the experimental results and calculations, the gap size is determined to be 230 nm to have the microring resonator in the slightly under-coupled regime, which are discussed in Section 2.3.

2.2 Device Fabrication

The SU-8 polymer microrings in this work are fabricated by NIL. Unlike the fabrication of the polymer microrings in our previous work where a silicon mold was used [18], in this work, a smooth-sidewall epoxysilsesquioxane (SSQ)-based transparent mold is used to imprint the device using a UV-imprinting technique. The transparent SSQ mold was duplicated from a smooth-sidewall silicon master mold, which was fabricated by using the combination of photoresist reflow method and continuous etching and passivation [30]. Once the transparent mold became fouled or damaged, a new mold could be prepared from the same master, which is a cost-effective method. And the UV-imprinting was helpful to lower the baking temperature which may bring wafer bending in a large-area NIL process. The UV-imprinting process started with spin coating of a SU-8 film (thickness: $\sim$150 nm) on a silicon substrate with a 4-μm thermal oxide layer on the top surface of the substrate. After the film was soft baked at 95 °C for 2 minutes, the imprinting was performed at pressure of $\sim$500 psi, temperature of $\sim$90 °C and UV energy $>$ 100 mJ/cm^2. Then, the demolding process was applied, and the sample was further baked at 95 °C for 2 minutes. Finally, an O_2 plasma etching process was applied to remove the residual layer. Fig. 3 shows the scanning electron microscope (SEM) images of the mold and the polymer microring resonator. In Fig. 3(a) and (b), we see that both the SSQ mold and the SU-8 microring have very smooth sidewalls. In Fig. 3(c), the top-view of a microring resonator is presented, and the gap size was measured to be 234 nm in Fig. 3(d), which agrees well with the design.

2.3 Device Characterization

Since a low detection limit requires a high Q factor and slightly under-coupled or critically-coupled operation for a microring resonator, it is necessary to characterize the device by analyzing its optical loss mechanism. The overall Q factor (Q_t) of the system is determined by Q_i and Q_c, and can be expressed as

$$\frac{1}{Q_t} = \frac{1}{Q_i} + \frac{1}{Q_c} \tag{2}$$

Fig. 4(a) shows the measured normalized transmission spectrum in deionized (DI) water. By fitting the spectrum, the sharp resonance notch has a linewidth of 1.29 pm, indicating an overall Q

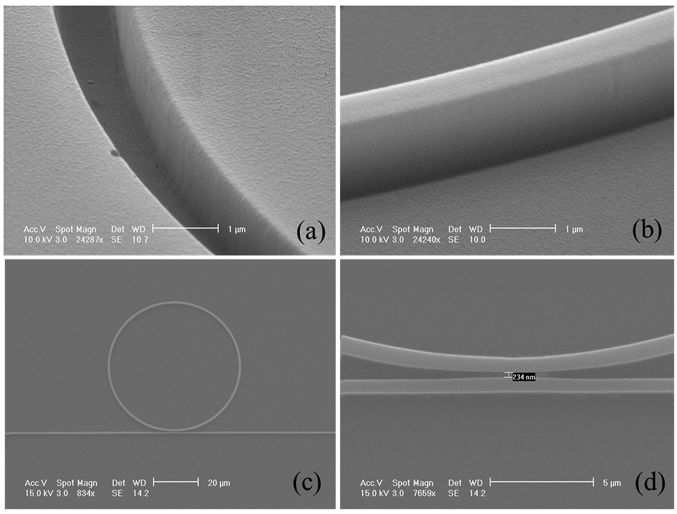

Fig. 3. SEM images of the mold and polymer microring resonotor: (a) sidewall of SSQ mold, (b) sidewall of SU-8 microring, (c) overall image of the microring, (d) zoom-in gap between the microring and the bus waveguide.

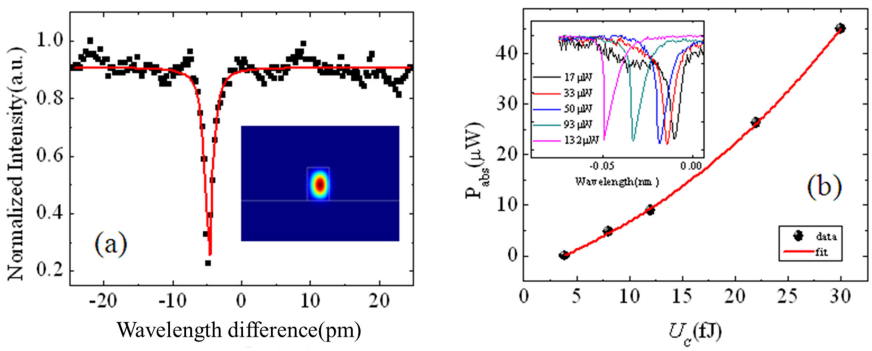

Fig. 4. (a) Normalized transmission spectrum of polymer microring. Inset: Simulated electrical field intensity distribution in the cross section of the polymer microring waveguide. (b) Relationship between intra-cavity energy U_c and absorbed power P_{abs}. Inset: Normalized transmission spectra of polymer micro-rings with different input power.

factor of 6.0×10^5. By fitting the data using Eq. (1), (Q_i, Q_c) are either (8.0×10^5, 2.4×10^6) or (2.4×10^6, 8.0×10^5).

To tell what coupled regime the device operates, it is necessary to analyze the factors that affect the Q_i factor. Q_i accounts for all the optical loss, including radiation loss, surface scattering loss, and material absorption loss. Thus, Q_i can be further expressed as

$$\frac{1}{Q_i} = \frac{1}{Q_r} + \frac{1}{Q_s} + \frac{1}{Q_a} \tag{3}$$

where Q_r, Q_s, and Q_a are radiation loss-related Q factor, surface scattering loss-related Q factor, and material absorption loss-related Q factor. Q_r is calculated by finite element method using COMSOL multi-physics software. The inset of Fig. 4(a) shows the electrical field intensity distribution of quasi-TE mode in the cross section of the polymer microring waveguide. We clearly see that the electrical filed is well confined in the ring waveguide region and only a very small amount of field leaks to the substrate. From the inset of Fig. 4(a), Q_r is calculated to be 4.5×10^6. Q_a can be extracted from the linear relation between the internal cavity energy and absorbed power [31].

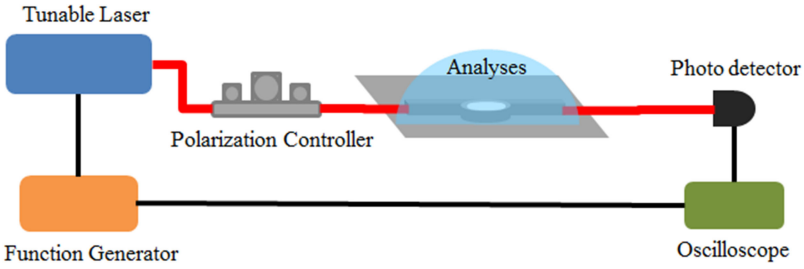

Fig. 5. The experimental setup.

When increasing the input power, the resonance notch shifts to a shorter wavelength and the line shape become asymmetric, as shown in the inset of Fig. 4(b), due to the negative value of the opto-thermal coefficient and the effect of thermal bistability due to the material absorption. The absorbed power, P_{abs}, is calculated from the thermal-induced wavelength shift, and the intra-cavity energy, U_c, is calculated by using the input power, Q factors and transmission spectra. Fig. 4(b) shows the relationship between P_{abs} and U_c. In the figure, a cubic polynomial fit ($P_{abs} \sim aU_c^3 + bU_c^2 + \gamma_{lin}U_c$) yields a linear material-absorption-related coefficient γ_{lin}, and therefore, the absorption-loss-related quality factor $Q_a = \omega/\gamma_{lin} = 3.1 \times 10^6$. Since $1/Q_i > 1/Q_r + 1/Q_a = 1/(1.8 \times 10^6) > 1/(2.4 \times 10^6)$, Q_i and Q_c should be 8.0×10^5 and 2.4×10^6, respectively, indicating that the microring is operated in the slightly under-coupled regime.

Further, Q_s can be calculated from Eq. (3), which is 1.4×10^6. Therefore, from this analysis, we believe that the Q factor of the SU-8 microring is limited by the surface scattering loss, which can be further improved by etching and reflow process in the future.

3. Experimental Setup and System Noises

3.1 Experiment Setup

The sensing characterization setup is shown in Fig. 5. The setup includes a tunable laser (New Focus TLB-6312, with a tuning range of 765 nm–781 nm), a function generator, a photodetector and an oscilloscope. A single mode fiber (Nufern 780-HP) and a conventional multimode fiber were coupled to the input and output ports of the bus waveguide, respectively. The polarization of the input light was controlled by a fiber based optical polarization controller, and TE polarization was used during the whole measurement. A triangular wave signal provided by the function generator was fed into the tunable laser to scan the laser wavelength, while the output light signal from the multimode fiber was received by the photodetector and then displayed on the oscilloscope. Note that the synchronization was provided by the function generator.

3.2 System Noise

The detection limit is determined by not only the Q factor of the device but also the noise of the system. Thus, it is important to achieve both high-Q microrings and a low-noise setup. The system noise comes from laser power instability, system desynchronization, uncompensated thermal fluctuation, limited oscilloscope bandwidth, photodetector noise and stray light of the environment. Since the thermo-optic coefficient of the SU-8 polymer is one order magnitude higher than that of silica, the SU-8 mircoring is more temperature-sensitive (roughly one order magnitude higher) than that of a typical silica resonator [32]. So the system temperature fluctuation was kept within 0.1 °C by a commercial thermoelectric cooler, in order to eliminate the thermal effect during the measurement. Here we characterize the system noise of the wavelength-shift-sensing scheme and the intensity-variation scheme. For the former scheme, the resonant wavelength shift is recorded every minute without changing the refractive index of the environment, as shown in Fig. 6(a). The

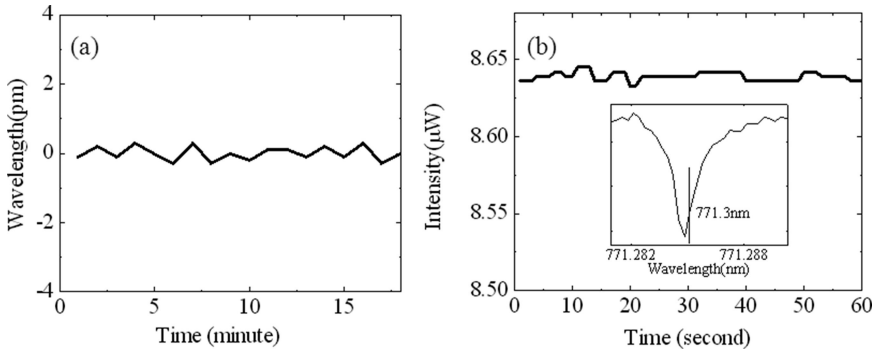

Fig. 6. Fluctuation of the signal versus time for (a) spectral measurement and (b) intensity measurement.

signal fluctuates slightly, and the standard deviation, δ_1, is 0.21 pm. For the latter scheme, the probing wavelength is fixed at 771.3 nm at the rising edge of the resonance, as shown in the inset of Fig. 6(b). With a low input optical power, the microring resonator is almost under thermal equilibrium condition, the intensity of output light signal from the multimode fiber was tracked and recorded every second, as shown in Fig. 6(b). The standard deviation of the signal, δ_2, is 2.90 nW (i.e., a fluctuation of 0.034%). Since the laboratory environment is very stable and the measured system noise is resulted by the combination of the various noise sources, we can infer that δ_1 could possibly result from the noise from the desynchronization of the tunable laser and the function generator, while the laser power instability, the photodetector noise, the limit of oscilloscope bandwidth could contribute to δ_2.

4. Characterization of Surface Mass Detection

In the surface mass detection, the evanescent field is used to detect the analytes adsorbed at the sensing surface. When bio or chemical analytes enter the evanescent field area of the optical mode near the surface, the effective refractive index (n_{eff}) of the resonant mode changes a little bit, leading to a tiny shift of the resonant wavelength.

First, we characterized the wavelength shift as the bulk RI changes. We immersed the device in water/ethanol solution of various concentrations. The reference transmission spectra of the device in DI water were measured every time when testing ethanol solutions of different concentrations. Fig. 7(a) shows the bulk refractive index sensitivity (BRIS) is 26.9 nm/RIU, which agrees well with the simulation result of 24.5 nm/RIU by using the COMSOL software.

Second, we measured the wavelength shift with different concentrations of BSA solutions. Then we prepared the BSA (molecular weight: 66 kDa) solution of various concentrations from 300 nM to 300 μM for the surface mass detection. The sensing surface was not functionalized, and thus, BSA molecules were physically adsorbed. The device was first rinsed with DI water. Then, it was immersed in the BSA solution. For each concentration of the BSA solution, we can see that the resonance shifts to a longer wavelength and then reaches the equilibrium. Fig. 7(b) presents the equilibrium spectra for different BSA concentrations. The resonance shift as a function of BSA concentrations is plotted in Fig. 7(c). Unlike the RI detection, the resonance shift increases nonlinearly with the increase of the BSA concentration. Note that for low-concentration BSA solutions, the WGM spectral shift has a linear dependence on the BSA concentration, as shown in the logarithmic plot in the inset of Fig. 7(c), where $\log(\Delta\lambda) \propto \log([BSA])$. This is in accordance with the relationship between the fraction (f) of the sites on the surface occupied by BSA over the whole surface and $[BSA]$, which is expressed as: $f = [BSA]/(K_d + [BSA])$, where K_d is the dissociation constant [33]. This is another evidence that the sensing mechanism is predominately the surface mass loading instead of the bulk refractive index change. After each measurement of one BSA concentration, the device was rinsed in DI water to remove the absorbed BSA in the solution. Then,

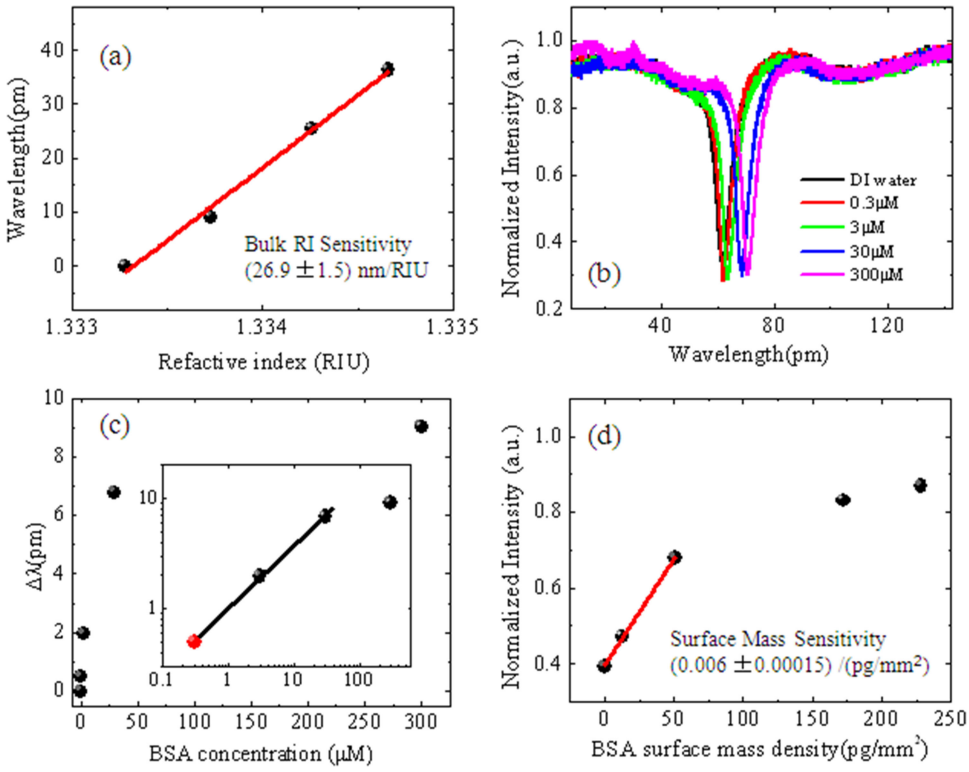

Fig. 7. (a) Resonance wavelength as a function of the change in liquid refractive index in the measurement. (b) Spectra shift due to the change of BSA concentration. (c) Resonance wavelength as a function of the BSA concentration change. Inset: log-log scale. Solid line is the linear fit in log-log scale. Red dot: detection limit for BSA concentration. (d) Intensity variation as a function of surface mass density.

the resonance of the device immersed in the DI water was measured again. We found that the resonance nearly went back to the reference, which shows that most of physically adsorbed BSA molecules were rinsed away from the surface.

Based on the theory described in Ref. [34], the average surface mass density σ can be expressed as

$$\sigma = -\frac{2\Delta\lambda \int \varepsilon_0 n^2 |E_0(r)|^2 dV}{\alpha_{ex}\lambda \int |E_0(r)|^2 dS} \tag{4}$$

where E_0 is the electrical field at the microring surface, α_{ex} is the excess polarizability of the BSA molecule [$\alpha_{ex} = 4\pi\varepsilon_0(3.85 \times 10^{-21}\ \text{cm}^3)$], n is refractive index, ε_0 is vacuum permittivity. The volume integral in the numerator is performed over the whole space of the microring waveguide while the surface integral in the denominator over the sidewalls and top surface. By calculating the optical mode with COMSOL software and by Eq. (4), the largest shift of 9.0 pm caused by 300 μM BSA corresponds to a BSA surface mass density of 228.5 pg/mm^2. Assuming a BSA molecule occupies an area 3.7×10^{-13} cm^2 [33], only 7.7% of the total surface of the microring resonator is covered with BSA. The low coverage in our results is mostly because BSA molecules are just physical adsorbed instead of molecule binding. The smallest spectral shift of 0.5 pm is shown in Fig. 7(c), which corresponds to a surface mass density of 12.7 pg/mm^2. The NEDL can thus be determined to be 5.3 pg/mm^2 [$= 12.7/0.5 \times 0.21$] considering the wavelength noise δ_1 of 0.21 pm.

Third, the intensity-variation scheme can also be used for sensing applications. By choosing the probing wavelength at the descending edge of the resonance dip (i.e., the position with a high slope), the surface mass density can be measured by observing the intensity variations, as

TABLE 1
Comparison Between Different Planar Microring Resonators for Surface Bio-Detection

Planar resonators	Q factor	Analytes	Detection limit	Ref.
Si microring	2×10^4	Avidin	10 ng/ml	[6]
Si microring	4.3×10^4	Streptavidin	60 fM	[7]
SiON microring	6×10^4	Aflatoxin	12.5nM	[17]
Polystyrene microring	2×10^4	Streptavidin	250 pg/mm^2	[20]
SU-8 microring	3.5×10^4	5-TAMRA cadaverine	0.05 fg/mm^2	[22]
SU-8 microring	6×10^5	Bovine serum albumin	12.7pg/mm^2	Our work

shown in Fig. 7(d). By fitting the data in the linear region (shown in the red curve in Fig. 7(d)), the sensitivity of the surface mass sensitivity of 0.006 /(pg/mm^2) can be obtained. Similarly, the NEDL can thus be estimated to be 55.9 fg/mm^2 [$=0.034\%/0.006 \times 10^3$] considering the intensity noise δ_2 of 2.9 nW (i.e., 0.034%). Compared with the NEDL by the wavelength-shift scheme, that by the intensity-variation scheme gives a much lower detection limit but a quite limited detection range. Table 1 summarizes the overall performance of various planar microring resonators for surface bio-detection. Our work shows that the high-*Q* microring has good biosensing performance without special surface functionalities.

5. Conclusions

In summary, we fabricated a polymer microring resonator that achieved the record-high intrinsic *Q* factor $\sim 8.0 \times 10^5$ by UV-imprinting technique. The systematic investigation of the microring resonator as a biosensing system shows its excellent performance even without special surface functionalities. In surface mass detection, a surface mass density of 12.7 pg/mm^2 of BSA was detected due to the physical adsorption. The NEDL is approximately 5.3 pg/mm^2 in the wavelength-shift scheme and 55.9 fg/mm^2 in the intensity-variation scheme. Using this mass fabrication, the ultrahigh-Q SU-8 microring resonator is an excellent and cost-effective platform for biosensing applications.

Acknowledgment

The authors would like to acknowledge instrument support from Electron Microbeam Analysis Laboratory (EMAL) and Lurie Nanofabrication Facility (LNF) in University of Michigan, Ann Arbor, MI, USA.

References

[1] X. Fan, I. M. White, S. I. Shopova, H. Zhu, J. D. Suter, and Y. Sun, "Sensitive optical biosensors for unlabeled targets: A review," *Anal. Chim. Acta*, vol. 620, no. 1, pp. 8–26, May 2008.
[2] A. N. Nordin, "Optical-resonator-based biosensing systems: Current status and future prospects," *Nanobiosensors Disease Diagnosis*, vol. 5, pp. 41–50, Jun. 2016.
[3] R. W. Boyd and J. E. Heebner, "Sensitive disk resonator photonic biosensor," *Appl. Opt.*, vol. 40, no. 31, pp. 5742–5747, Nov. 2001.
[4] S. M. Grist *et al.*, "Silicon photonic micro-disk resonators for label-free biosensing," *Opt. Exp.*, vol. 21, no. 7, pp. 7994–8006, Apr. 2013.
[5] A. Yalcin *et al.*, "Optical sensing of biomolecules using microring resonators," *IEEE J. Sel. Top. Quantum Electron.*, vol. 12, no. 1, pp. 148–155, Feb. 2006.
[6] K. D. Vos, I. Bartolozzi, E. Schacht, P. Bienstman, and R. Baets, "Silicon-on-insulator microring resonator for sensitive and label-free biosensing," *Opt. Exp.*, vol. 15, no. 12, pp. 7610–7615, Jun. 2007.
[7] M. Iqbal *et al.*, "Label-free biosensor arrays based on silicon ring resonators and high-speed optical scanning instrumentation," *IEEE J. Sel. Top. Quantum Electron.*, vol. 16, no. 3, pp. 654–661, Mar. 2010.
[8] F. Vollmer, D. Braun, A. Libchaber, M. Khoshsima, I. Teraoka, and S. Arnold, "Protein detection by optical shift of a resonant microcavity," *Appl. Phys. Lett.*, vol. 80, no. 21, pp. 4057–4059, May 2002.

[9] A. M. Armani, R. P. Kulkarni, S. E. Fraser, R. C. Flagan, and K. J. Vahala, "Label-free, single-molecule detection with optical microcavities," *Science*, vol. 317, no. 5839, pp. 783–787, Aug. 2007.
[10] H. Li and X. Fan, "Characterization of sensing capability of optofluidic ring resonator biosensors," *Appl. Phys. Lett.*, vol. 97, Jul. 2010, Art. no. 011105.
[11] Y. Guo, H. Li, K. Reddy, H. S. Shelar, V. R. Nittoor, and X. Fan, "Optofluidic Fabry–Pérot cavity biosensor with integrated flow-through micro-/nanochannels," *Appl. Phys. Lett.*, vol. 98, Jan. 2011, Art. no. 041104.
[12] E. Chow, A. Grot, L. W. Mirkarimi, M. Sigalas, and G. Girolami, "Ultracompact biochemical sensor built with two-dimensional photonic crystal microcavity," *Opt. Lett.*, vol. 29, no. 10, pp. 1093–1095, May 2004.
[13] M. Lu, S. S. Choi, U. Irfan, and B. T. Cunningham, "Plastic distributed feedback laser biosensor," *Appl. Phys. Lett.*, vol. 93, Sep. 2008, Art. no. 111113.
[14] M. R. Foreman, J. D. Swaim, and F. Vollmer, "Whispering gallery mode sensors," *Adv. Opt. Photon.*, vol. 7, no. 2, pp. 168–240, May. 2015.
[15] N. Jokerst, M. Royal, S. Palit, L. Luan, S. Dhar, and T. Tyler, "Chip scale integrated microresonator sensing systems," *J. Biophoton.*, vol. 2, no. 4, pp. 212–226, Apr. 2009.
[16] M. Bahadoran *et al.*, "Modeling and analysis of a microresonating biosensor for detection of Salmonella bacteria in human blood," *Sensors*, vol. 14, no. 7, pp. 12885–12899, Jul. 2014.
[17] R. Guider *et al.*, "Design and optimization of SiON ring resonator-based biosensors for aflatoxin M1 detection," *Sensors*, vol. 15, no. 7, pp. 17300–17312, Jul. 2015.
[18] C.-Y. Chao and L. J. Guo, "Polymer microring resonators fabricated by nanoimprint technique," *J. Vac. Sci. Technol. B*, vol. 20, no. 6, pp. 2862–2866, Dec. 2002.
[19] S. Cho and N. M. Jokerst, "A polymer microdisk photonic sensor integrated onto silicon," *IEEE J. Lightw. Technol.*, vol. 18, no. 20, pp. 2096–2098, Oct. 2006.
[20] C.-Y. Chao, W. Fung, and L. J. Guo, "Polymer microring resonators for biochemical sensing applications," *IEEE J. Sel. Top. Quantum Electron.*, vol. 12, no. 1, pp. 134–142, Feb. 2006.
[21] G.-D. Kim, G.-S. Son, H.-S. Lee, K.-D. Kim, and S.-S. Lee, "Integrated photonic glucose biosensor using a vertically coupled microring resonator in polymers," *Opt. Commun.*, vol. 281, no. 18, pp. 4644–4647, Sep. 2008.
[22] C. Delezoide *et al.*, "Vertically coupled polymer microracetrack resonators for label-free biochemical sensors," *IEEE Photon. Technol. Lett.*, vol. 24, no. 4, pp. 270–272, Feb. 2012.
[23] M. Mancuso, J. M. Goddard, and D. Erickson, "Nanoporous polymer ring resonators for biosensing," *Opt. Exp.*, vol. 20, no. 1, pp. 245–255, Jan. 2012.
[24] M. H. M. Salleh, A. Glidle, M. Sorel, J. Reboud, and J. M. Cooper, "Polymer dual ring resonators for label-free optical biosensing using microfluidics," *Chem. Commun.*, vol. 49, no. 30, pp. 3095–3097, Jan. 2013.
[25] P. Girault *et al.*, "Integrated polymer micro-ring resonators for optical sensing applications," *J. Appl. Phys.*, vol. 117, no. 10, Mar. 2015, Art. no. 104504.
[26] R. Morarescu *et al.*, "Fabrication and characterization of high-optical-quality-factor hybrid polymer microring resonators operating at very near infrared wavelengths," *IEEE Photon. J.*, vol. 8, no. 2, Apr. 2016, Art no. 6600409.
[27] A. V. Shneidman *et al.*, "All-polymer integrated optical resonators by roll-to-roll nanoimprint lithography," *ACS Photon.*, vol. 5, no. 5, pp. 1839–1845, Apr. 2018.
[28] C.-Y. Chao and L. J. Guo, "Design and optimization of microring resonators in biochemical sensing applications," *IEEE J. Lightw. Technol.*, vol. 24, no. 3, pp. 1395–1402, Mar. 2006.
[29] B. E. Little, S. T. Chu, H. A. Haus, J. Foresi, and J. Laine, "Microring resonator channel dropping filters," *IEEE J. Lightw. Technol.*, vol. 15, no. 6, pp. 998–1005, Jun. 1997.
[30] T. Ling, S.-L. Chen, and L. J. Guo, "Fabrication and characterization of high Q polymer micro-ring resonator and its application as a sensitive ultrasonic detector," *Opt. Exp.*, vol. 19, no. 2, pp. 861–869, Jan. 2011.
[31] M. Borselli, T. J. Johnson, and O. Painter, "Beyond the Rayleigh scattering limit in high-Q silicon microdisks: Theory and experiment," *Opt. Exp.*, vol. 13, no. 5, pp. 1515–1530, Mar. 2005.
[32] S. Dass and R. Jha, "Square knot resonator-based compact bending sensor," *IEEE Photon. Technol. Lett.*, vol. 30, no. 18, pp. 1649–1652, Jul. 2018.
[33] H. Zhu, I. M. White, J. D. Suter, P. S. Dale, and X. Fan, "Analysis of biomolecule detection with optofluidic ring resonator sensors," *Opt. Exp.*, vol. 15, no. 15, pp. 9139–9146, Jul. 2007.
[34] S. Arnold, M. Khoshsima, I. Teraoka, S. Holler, and F. Vollmer, "Shift of whispering-gallery modes in microspheres by protein adsorption," *Opt. Lett.*, vol. 28, no. 4, pp. 272–274, Feb. 2003.